# Mechanically reprogrammable Pancharatnam–Berry metasurface for microwaves

**Quan Xu [ID],[a] Xiaoqiang Su,[b,*] Xueqian Zhang,[a] Lijuan Dong,[b] Lifeng Liu,[b] Yunlong Shi,[b] Qiu Wang,[c] Ming Kang,[d] Andrea Alù [ID],[e,f] Shuang Zhang [ID],[g,h,*] Jiaguang Han,[a,i,*] and Weili Zhang [ID][j,*]**

[a]Tianjin University, Center for Terahertz Waves and College of Precision Instrument and Optoelectronics Engineering, Key Laboratory of Optoelectronic Information Technology (Ministry of Education of China), Tianjin, China
[b]Shanxi Datong University, Institute of Solid State Physics and College of Physics and Electronic Science, Shanxi Province Key Laboratory of Microstructure Electromagnetic Functional Materials, Datong, China
[c]Wuhan University of Technology, School of Information Engineering, Wuhan, China
[d]Tianjin Normal University, College of Physics and Materials Science, Tianjin, China
[e]City University of New York, Advanced Science Research Center, Photonics Initiative, New York, United States
[f]City University of New York, Graduate Center, Physics Program, New York, United States
[g]University of Hong Kong, Faculty of Science, Department of Physics, Hong Kong, China
[h]University of Hong Kong, Department of Electrical and Electronic Engineering, Hong Kong, China
[i]Guilin University of Electronic Technology, Guangxi Key Laboratory of Optoelectronic Information Processing, School of Optoelectronic Engineering, Guilin, China
[j]Oklahoma State University, School of Electrical and Computer Engineering, Stillwater, Oklahoma, United States

**Abstract.** Metasurfaces have enabled the realization of several optical functionalities over an ultrathin platform, fostering the exciting field of flat optics. Traditional metasurfaces are achieved by arranging a layout of static meta-atoms to imprint a desired operation on the impinging wavefront, but their functionality cannot be altered. Reconfigurability and programmability of metasurfaces are the next important step to broaden their impact, adding customized on-demand functionality in which each meta-atom can be individually reprogrammed. We demonstrate a mechanical metasurface platform with controllable rotation at the meta-atom level, which can implement continuous Pancharatnam–Berry phase control of circularly polarized microwaves. As the proof-of-concept experiments, we demonstrate metalensing, focused vortex beam generation, and holographic imaging in the same metasurface template, exhibiting versatility and superior performance. Such dynamic control of electromagnetic waves using a single, low-cost metasurface paves an avenue towards practical applications, driving the field of reprogrammable intelligent metasurfaces for a variety of applications.

Key words: reprogrammable metasurfaces; Pancharatnam–Berry phase; mechanical metasurfaces; microwaves.

## 1 Introduction

As one of the most rapidly expanding frontiers of modern photonics, metasurfaces hold promise for a wide range of applications due to their compact physical size and unconventional optical functionalities.[1–6] These flat and miniaturized devices usually consist of an array of optically thin meta-atoms (plasmonic or dielectric structures) with spatially varying geometrical parameters and subwavelength separations aimed at imprinting on the incoming optical wavefront a functionality[7–12] of choice through tailored local interactions of the phase,[13–15] amplitude,[16–18] and polarization.[19–21] The further development of this field entails not only endeavors to optimize the static metasurface performance for certain functionalities[22–24] but also

*Address all correspondence to Xiaoqiang Su, xiaoqiang.su@sxdtdx.edu.cn; Shuang Zhang, shuzhang@hku.hk; Jiaguang Han, jiaghan@tju.edu.cn; Weili Zhang, weili.zhang@okstate.edu

most importantly techniques for tunable/reprogrammable meta-surfaces that can be flexibly controlled on demand and in real time.[25–27] In the terahertz and optical regimes, dynamic meta-surfaces have mainly been achieved by utilizing the response of tunable materials to external stimuli, such as optical pump,[28–31] heating,[32–34] and bias voltage.[35–38] Nevertheless, limited by the current techniques of fabrication and modulation, these metasurfaces have been limited to simultaneous tuning of a large portion of the meta-atoms, and thus can only be switched among a limited number of operations.

In the microwave regime, PIN diodes and varactor diodes have been recently used to design reprogrammable metasurfaces with individually reconfigured meta-atoms,[39–54] due to their miniaturized sizes compatible with passive metallic resonators. By judicious designs, several dynamic functionalities including holographic imaging,[39] special beam steering,[41,43,48,53] and topological surface state control[50] have been demonstrated. Moreover, digital and real-time features promote several system-level applications that can hardly be achieved by static metasurfaces, such as space-time-coding,[42,44,54] intelligent autonomous self-adaptive systems,[40,45,46] and dynamic optimization of wireless communication channels.[47,49,51] Despite this progress, the degrees of freedom of PIN diode-based meta-atoms have been limited to two or four phase levels per meta-atom, i.e., the reprogrammability was limited to a locally controllable abrupt phase by a step of $\pi$ or $\pi/2$ at best. This limitation causes a roughly discontinuous phase distribution that unavoidably introduces diffraction losses. Meanwhile, it also limits the amount of information that can be processed by a metasurface of given size.[55] Programmable metasurfaces utilizing varactor diodes can enable phase levels larger than four;[41,46,53] however, their operation was based on the dynamic phase around a resonance dip,[38] resulting in the significant amplitude variation when adjusting the phase response. To eliminate such amplitude-phase correlation-induced distortion in specific wavefront control, due consideration should be paid into inverse design optimization algorithms.[56,57] Moreover, each meta-atom in electrically or optically reprogrammable metasurfaces requires at least one PIN diode, photodiode, or varactor diode,[39–54] whose typical power dissipation is about several hundred milliwatts, and they need a continuous power supply to maintain the functionality. Such energy consumption entails a trade-off between the size/number of meta-atoms and the overall metasurface size, hindering large-scale applications.

Notably, the shortcomings of the above-discussed microwave metasurfaces, including the meta-atom capability and the energy consumption, are mainly resulting from the limitations of the adopted voltage-driven elements. Improving the electrical metric of PIN diodes and varactor diodes, no doubt can optimize the metasurface performance, but it is an even harder challenge in electronic engineering, especially for higher frequencies.[58] As thus, researchers have also carried out studies on the other physical mechanisms for achieving reconfigurable metasurfaces. For example, it has been demonstrated that an array of cavities can be filled with liquid mercury in a controllable manner using microfluidic technology in which the overall electromagnetic response can be tailored for different functionalities.[59] In addition, origami[60] and mechanical lifting[61] approaches have also been reported for achieving reconfigurable metasurfaces where each of the meta-atoms is spatially folded/unfolded or lifted/dropped to tailor the overall metasurface functionality. Such approaches,[59–61] free from voltage-driven elements inside

meta-atoms, hold an advantage of nonvolatility that the maintaining of designated functionality does not consume electricity. These works have played an important role in exploring the reconfigurable metasurfaces; however, the wavefront control capability remains insufficient.

In this article, we propose and demonstrate a reprogrammable metasurface platform based on mechanical control for quasicontinuous Pancharatnam–Berry (PB) phase tunability operating at microwave frequencies. PB phase,[7,8,62,63] also known as geometric phase, is a robust control method for incident circularly polarized waves, which is determined by the rotation angle of meta-atoms and it is therefore decoupled from amplitude control. Figure 1(a) schematically shows our reprogrammable PB metasurface platform, which consists of $20 \times 20$ supercells covering an area of 870 mm × 870 mm. Each supercell, as shown in Fig. 1(b), is composed of a stepping motor, a set of transmission gears, and an array of $4 \times 4$ PB meta-atoms. The reprogrammable function is enabled by mechanically rotating each PB meta-atom to achieve the desired phase control, enabling a continuous and arbitrary phase control pattern over the entire surface with a high-efficiency and uniform amplitude. In principle, this metasurface platform can be employed for on-demand generation of a large variety of functionalities in real time. As proof-of-concept experiments, we demonstrate metalensing, focused vortex generation, and holographic imaging using the same metasurface, exhibiting superior performance and real-time tunability.

## 2 Materials and Methods

### 2.1 Design of the Reprogrammable Metasurface

To empower the metasurface with well-controlled programmability, 400 commercial stepping motors are utilized to respectively control the $20 \times 20$ supercells. Each stepping motor is equipped with an addressed circuit for the power supply (terminal voltage of 5 V) and rotation control. The step angle is 5.625 deg, corresponding to 64 steps per turn. More details about the stepping motor can be found in Supplementary Material 1. The rotation step number (clockwise or counterclockwise) of each motor is controlled by wireless signals from a host computer with full addressability. As shown in Fig. 1(b), a three-layered gear set is utilized to transmit the torque from the motor to the PB meta-atoms: the first layer consists of the main gear attached to the output shaft of the stepping motor; the middle layer consists of four gears that connect the first and last layers; and the bottom layer consists of 16 gears connecting with the PB meta-atoms one by one. The modules of all gears are 0.5. The yellow-green gear has 30 teeth, the light-blue gear has 30 and 16 teeth in the bottom and top layers, respectively, and the pink gear has 14 teeth. In this condition, when the stepping motor rotates a turn, it drives the PB meta-atoms to rotate 8/7 turns. Accordingly, the rotation of each meta-atom consists of 56 steps per turn. For reference, Supplemental Video S1 (MP4, 30 MB [URL: https://doi.org/10.1117/1.AP.4.1.016002.1]) is provided to show the controllable rotations. The photos of the metasurface template and more details about each component can be found in Supplementary Material 2.

Different from traditional static metasurfaces, the meta-atoms of the proposed reprogrammable metasurface are discretely arranged to avoid possible obstructions during their rotation. With the overall performance taken into consideration, a
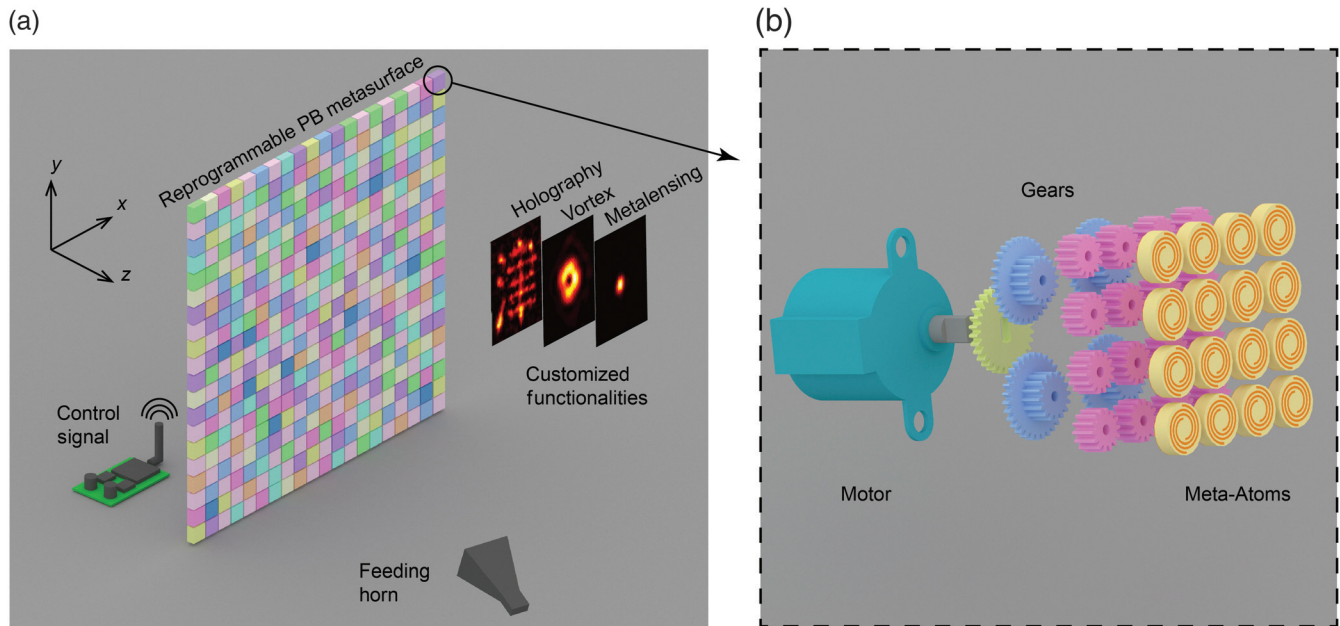
**Fig. 1** Schematics of the metasurface and its supercell. (a) The metasurface is formed by an array of supercells, arranged in a square lattice with a period of 43.5 mm. The PB phase response of each supercell is controlled by an addressable wireless signal and can be independently tuned over 28 phase levels. The metasurface can be reprogrammed to realize custom functionalities including metalensing, focused vortex beam generation, and holographic imaging by a proper design of the PB phase distribution. (b) The PB phase control in each supercell is achieved by transmitting the torque from a stepping motor to the PB meta-atoms through a set of gears.

circular-shaped metal–insulator–metal structure, as schematically shown in Fig. 2(a), is chosen as the meta-atom to manipulate the PB phase in reflection at an operating frequency of 7 GHz (see Supplementary Material 3 for simulation details). The PB meta-atom consists of two Archimedean spirals with the same geometric parameters, which are C2 rotation-symmetric with each other along the normal axis. Both the spirals and the bottom metallic film are made from 35-$\mu$m thick copper. They are fabricated using standard printed circuit board technology over a 3-mm-thick FR4 substrate, with relative permittivity of 4.2 and a loss tangent of 0.025. The radius of the meta-atom is $R = 4.8$ mm and the center distance between adjacent meta-atoms along the $x$ and $y$ directions is about 10.7 mm, leaving a minimum distance of about 1.1 mm to ensure smooth rotation of each meta-atom. Two important features characterize the chosen PB meta-atom in its interaction with the incident light: it provides strong anisotropy to achieve efficient polarization conversion, and it can strongly confine the resonance fields inside the meta-atom to minimize near-field coupling between neighboring meta-atoms (see Supplementary Material 3 for details). By carefully optimizing the meta-atom dimensions, such meta-atoms could efficiently convert the incident right- and left-handed circular polarizations (RCP and LCP) to reflected RCP and LCP, respectively. In principle, when this meta-atom is rotated by an angle $\theta$, the phases of reflected $R_{rr}$ and $R_{ll}$ (the subscripts $r$ and $l$ stand for RCP and LCP) are expected to follow a phase gradient of $2\theta$ and $-2\theta$, respectively, where the sign depends on the spin direction of incident polarization. Such geometric-dependent phase behavior is also known as the PB phase response.[7,8,62,63]

### 2.2 Experimental Verification of PB Phase Controllability

Since the PB meta-atom can be rotated by 56 steps per turn, our metasurface enables quasicontinuous PB phase control over 28 levels. As schematically shown by the pink and sky-blue dials in Fig. 2(a), the reflectance $R_{rr}$ and $R_{ll}$ have a phase control resolution of $\pi/14$ and opposite phase gradients. To experimentally characterize the metasurface, an experimental setup is established by a vector network analyzer (VNA, Agilent N5230C) and two broadband horn antennas (see Appendix). Figures 2(b) and 2(c) show the normalized amplitude of measured $R_{rr}$ and $R_{ll}$, respectively, where the amplitude peak around the target working frequency of 7 GHz can be obtained in both spectra. $|R_{rr}|$ has a maximum amplitude of 0.91 at 6.925 GHz and $|R_{ll}|$ has a maximum amplitude of 0.7 at 6.55 GHz. Notably, when light impinges onto a chiral meta-atom that lacks mirror-symmetry, photons of different CPs will undergo different absorption, an effect known as circular dichroism or circular conversion dichroism.[24] The chosen PB meta-atom shows a chiral response, thus we expect a difference between $R_{rr}$ and $R_{ll}$, as shown in Fig. 2. For different applications, one can either design a PB meta-atom with in-plane mirror-symmetry to eliminate circular conversion dichroism[7] or design chiral PB meta-atoms with stronger symmetry breaking to enhance circular conversion dichroism.[64] The red and blue circles in Figs. 2(d) and 2(e) illustrate the measured phase response of $R_{rr}$ and $R_{ll}$, respectively, at 7 GHz, as we simultaneously rotate all meta-atoms from 0 to $\pi$. Clearly, the phase variation of $R_{rr}$ and $R_{ll}$ has a positive and negative gradient versus the rotation angle, respectively. The solid lines in Figs. 2(d)
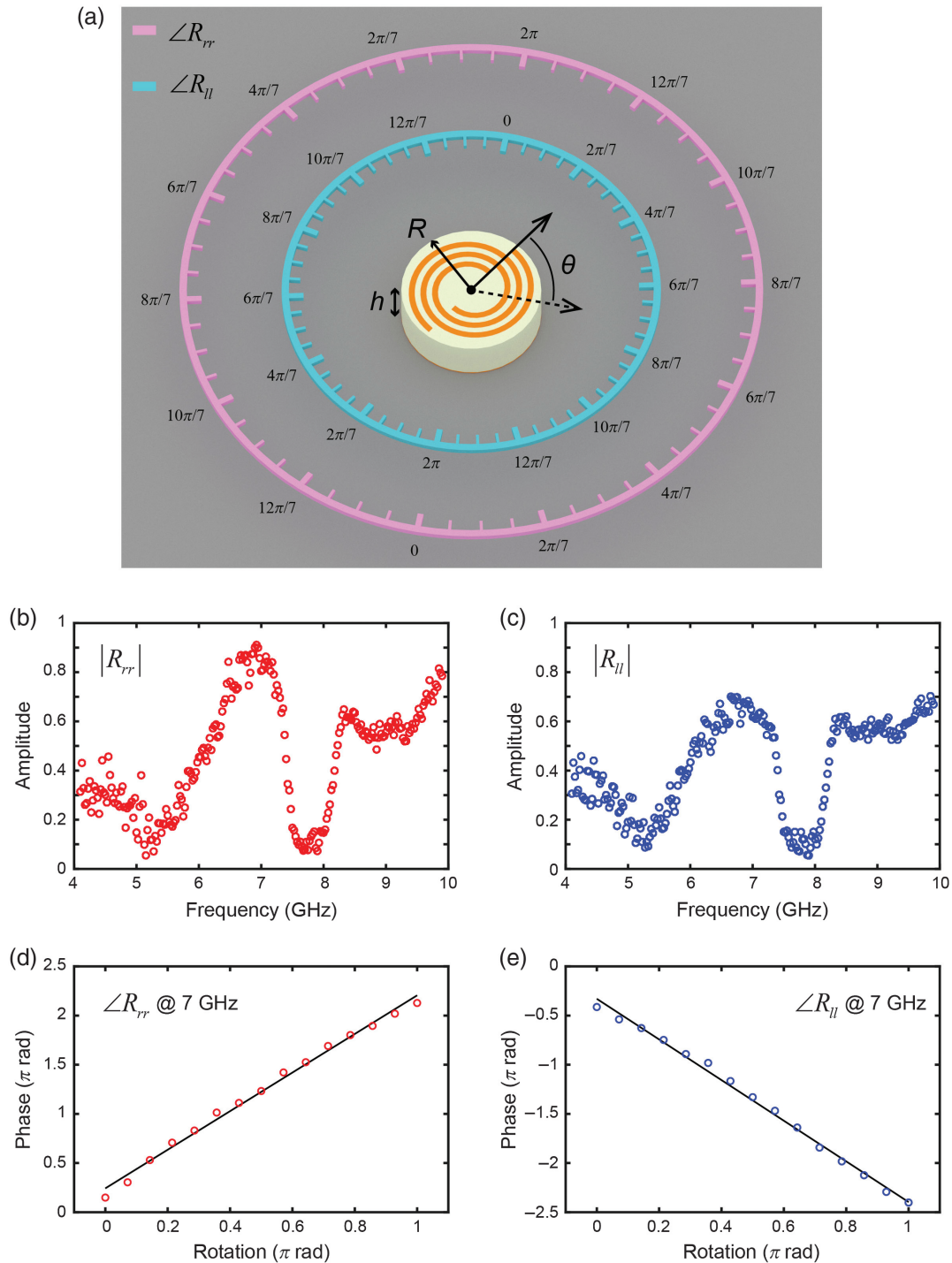
**Fig. 2** PB phase response. (a) The top portion of the PB meta-atom is a pair of Archimedean spirals with the same geometric parameters: inner radius (1.9 mm), outer radius (4.3 mm), height (0.035 mm), width (0.4 mm), and number of turns (two turns). The pink and sky-blue dials schematically depict the PB phase control resolution and variation gradients for $R_{rr}$ and $R_{ll}$, respectively. (b), (c) Measured amplitudes of $R_{rr}$ and $R_{ll}$, respectively. (d), (e) Measured PB phase response of $R_{rr}$ and $R_{ll}$, respectively, versus different rotation angles.

and 2(e) show the linearly fitted results, where the fitting gradient of $R_{rr}$ and $R_{ll}$ is 1.9624 and −2.0665, respectively, which agree well with the theoretical value. In addition, Fig. S4 in the Supplementary Material shows the measured phase responses at 6, 6.7, and 7.4 GHz, which also comply well with the PB phase response. These results experimentally verify the PB phase controllability of the proposed metasurface platform in a broad band.

### 2.3 Rotation Distribution Design for Reprogrammable Optical Functionality

Since each supercell can be individually controlled, the metasurface yields a variety of optical functionalities by designing the rotation distribution over the surface. We define the metasurface as the *xy*-plane and its center the origin of our coordinate system. To experimentally characterize the performance, a broadband antenna is coaxially mounted at (0, 0, 2100 mm) as a feeding source, and a waveguide probe is used to scan the electric filed distribution (see Appendix). Since the wave emitted by the antenna is not a plane wave as it reaches the metasurface, we should compensate its phase to make it collimated (see Supplementary Material 5 for details). Notably, due to the quasicontinuous phase controllability, our metasurface can flexibly work under various incident wavefronts, since the functionality distortion produced by a nonplanar incident wavefront can be easily compensated. Such flexibility is quite important in

practical applications, especially in scenarios in which the feeding antenna can hardly be placed in the Fraunhofer region of the metasurface.[39,42] Once the desired phase distribution for certain target functionality is obtained, the corresponding rotation distribution can be calculated. In the following, we choose RCP as target operating polarization to demonstrate several representative functionalities, including metalensing, focused vortex beam generation, and holographic imaging.

## 3 Results

### 3.1 Metalensing

We first investigate the functionality of a metalens using the proposed metasurface. Figure 3(a) shows the required rotation profile for a metasurface focusing the impinging wave at (0, 0, 600 mm). The measured electric field intensity ($|R_{rr}|^2$) in the *xy*-plane at $z = 600$ mm is shown in Fig. 3(b), where a highly
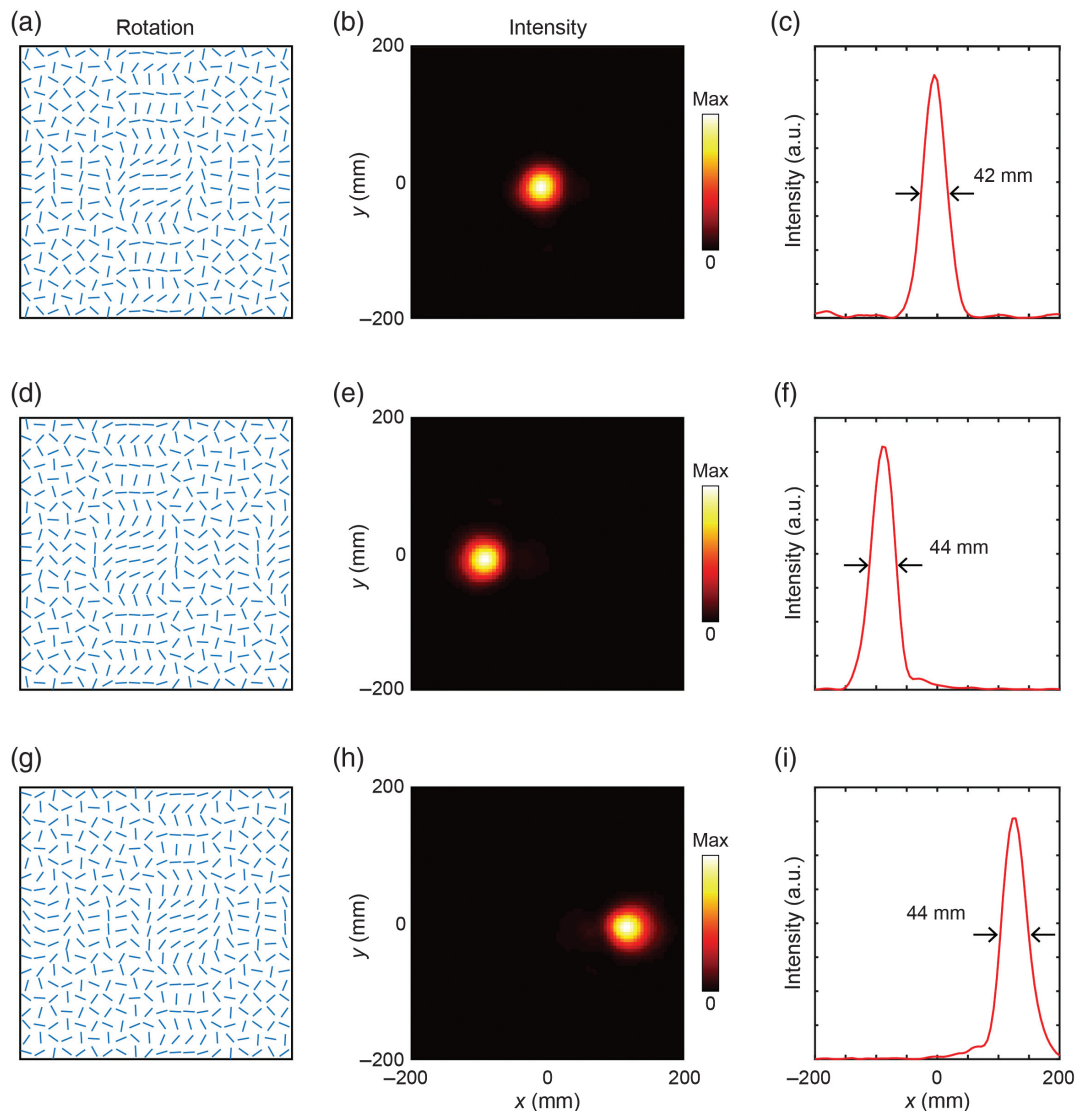


**Fig. 3** Realization of metalensing. (a), (d), (g) Required rotation profiles to realize different metalens operations for RCP waves. (b), (e), (h) Measured electric field intensities ($|R_{rr}|^2$) at 7 GHz on the focal plane. (c), (f), (i) Horizontal cuts of the metalens focal spots, with FWHMs = 42, 44, and 44 mm, respectively.

symmetric focal spot can be obtained. The horizontal cut of the focal spot is shown in Fig. 3(c) showing a full-width at half-maximum (FWHM) ~42 mm. Notably, the numerical aperture of the demonstrated metalens is about 0.587, corresponding to a diffraction-limited FWHM of ~36.5 mm at 7 GHz. We remark that the generated focal spot is quite close to the diffraction limit, indicating the excellent performance of our quasicontinuous phase control. The programmability of our metasurface enables scanning the focus off-axis. Figures 3(d) and 3(g) show the desired rotation profiles for focusing at $(-80, 0, 600 \text{ mm})$ and $(120, 0, 600 \text{ mm})$, respectively. The measured electric field intensities and the horizontal cuts of the focal spots are shown in Figs. 3(e), 3(h) and 3(f), 3(i), respectively, to perform very well in terms of their focusing and scanning capabilities. In addition, lensing with continuously varying focal lengths can also be achieved. For example, Fig. S6 in the Supplementary Material shows experimentally measured focusing at $(0, 0, 450 \text{ mm})$, $(0, 0, 600 \text{ mm})$, and $(0, 0, 750 \text{ mm})$, respectively. These high-quality and compact focal spots experimentally verify the accuracy of the phase realization of our proposed metasurface.

## 3.2 Focused Vortex Generation

Electromagnetic fields with a phase profile $e^{il\varphi}$ carry orbital angular momentum (OAM), where $\varphi$ is the azimuthal coordinate in the transverse plane and $l$ is the topological charge. To corroborate the generality of the proposed metasurface, we show reprogrammable focused vortex generations in Fig. 4. These vortices are designed to coaxially focus at $(0, 0, 600 \text{ mm})$, thus their target rotation angle distribution is the one in Fig. 3(a) plus $l/2$ times the azimuthal angle. Figures 4(a), 4(e), 4(i), and 4(m) show the required rotation distribution across the surface to generate focused vortex beams of topological charges $l = 1, 2, 3, 4$, respectively. Figures 4(b), 4(f), 4(j), and 4(n) show the measured electric intensity $(|R_{rr}|^2)$ distributions of the vortex beams, respectively, at the focal plane $z = 600 \text{ mm}$. As expected, these intensity distributions exhibit doughnut shapes, and the central dark area of the vortices is larger for increased topological charge. Figures 4(c), 4(g), 4(k), and 4(o) show the corresponding measured phase distributions, where the azimuthal angle dependence clearly reveals the vortex nature of the focused beams. To quantitatively analyze the quality of the vortex beams, we extracted and integrated the complex amplitudes to get the amplitude $|S_n|$ of each OAM (see Supplementary Material 7 for details). Figures 4(d), 4(h), 4(l), and 4(p) show the corresponding normalized $|S_n|$ as a function of $l$ from $-6$ to 6, respectively. Clearly, the target OAM component of each measurement is the strongest, whereas the other OAM components are quite weak, indicating the high purity of the generated vortex beams. The existence of unwanted OAM beams can be attributed to the square shape of the metasurface and the experimental errors (see Supplementary Material 8 for details). These results experimentally illustrate the large reprogrammability and at the same time high efficiency of our metasurface in tailoring the impinging fields at will.

## 3.3 Holographic Imaging

Metasurface holography has become a well-established approach to address inverse engineering problems for electromagnetic waves. To further explore the wavefront control capability of our programmable metasurface, we apply it to construct computer-generated holographic images in Fig. 5. In our demonstration, the Chinese characters "天津大学" (Tianjin University) and "大同云冈" (Datong Yungang) were generated in the image plane at $z = 600 \text{ mm}$. The required rotation profile for each word, as shown in Figs. 5(a)–5(d) and 5(i)–5(l), was calculated by a modified Gerchberg–Saxton algorithm,[64,65] in which the conventionally used Fresnel diffraction formula is replaced by the Rayleigh–Sommerfeld diffraction formula (see Supplementary Material 9 for details). To confirm the functionality, we calculated the holography imaging by considering the meta-atoms as point sources with ideally designated hologram phase profiles. The calculated results are shown in Fig. S9 in the Supplementary Materials, which comply well with the target characters. To experimentally demonstrate these holographic images, we rotated the meta-atoms according to the required rotation profile and measured the corresponding electric intensity $(|R_{rr}|^2)$ distribution. Although the holograms have only $20 \times 20$ pixelated phase points, the generated holographic images, as shown in Figs. 5(e)–5(h) and 5(m)–5(p), are of very high-quality and in good agreement with calculations, indicating the excellent wavefront control capability of the proposed reprogrammable metasurface platform.

## 3.4 Polarization-Sensitivity Manipulation

Polarization sensitivity is an important feature of metasurfaces. Since the proposed metasurface is based on the PB phase concept, once all the meta-atoms are arranged to achieve the desired phase profile $\Phi$ for specific functionality under LCP (RCP) incidence, the corresponding phase profile under RCP (LCP) incidence turns to $\Phi' = -\Phi$. In most cases, the phase profile of $\Phi'$ cannot maintain the same functionality as that of $\Phi$. For instance, Fig. S10 in the Supplementary Material shows the measurements in the case of the metasurface are designated to generate a holographic image of the word "PB" under an LCP incidence, where the measured $|R_{ll}|^2$ successfully forms the holographic image while the measured $|R_{rr}|^2$ is very noisy. Similarly, the demonstrated functionalities shown in Figs. 3–5 are also polarization-sensitive and limited to work for RCP. Inspired by a recent work that utilized binary geometric phase control to achieve polarization-insensitive metalensing in the visible range,[66] we find that the proposed metasurface can also maintain the same functionality for multipolarizations. For instance, Fig. S11 in the Supplementary Material shows the rotation profile of meta-atoms to achieve metalensing at $(0, 0, 600 \text{ mm})$, where the orientation angles are binarily arranged with $-\pi/4$ and $\pi/4$. In this condition, the reflected intensity profiles of $|R_{rr}|^2$, $|R_{ll}|^2$, $|R_{xy}|^2$, and $|R_{yx}|^2$ can focus at the same spot, as shown in Fig. S11f-I in the Supplementary Material.

In addition, the polarization-dependence and wavelength-independence of PB phase control can be further exploited to achieve polarization and frequency multiplexed functionalities.[67] For achieving functionality under RCP for wavelength $\lambda_1$, the desired phase distribution can be calculated as $\Phi_{R,1}$. Similarly, for achieving other functionality under LCP for wavelength $\lambda_2$, the desired phase distribution can be calculated as $\Phi_{L,2}$. To multiplex these phase distributions into one set of meta-atoms, one can arrange the rotation profile as $\theta = \arg[\exp(i\Phi_{R,1}) + \exp(-i\Phi_{L,2})]/2$. In this condition, under RCP incidence the metasurface will perform the phase profiles of $\Phi_{R,1}$ and $-\Phi_{L,2}$, and similarly under LCP incidence the metasurface will perform the phase profiles of $-\Phi_{R,1}$ and $\Phi_{L,2}$.
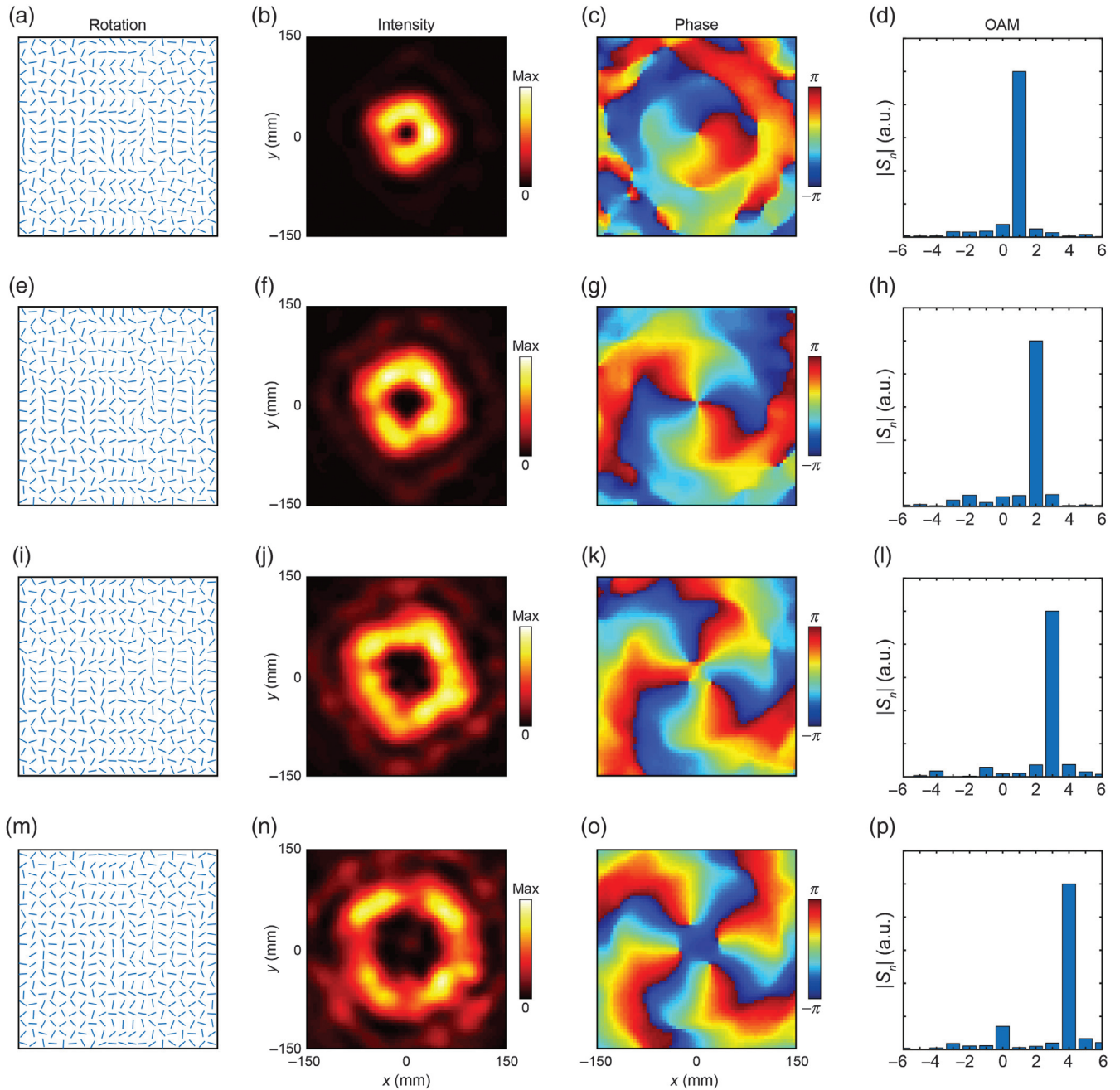
**Fig. 4** Focused vortex beam generation. (a), (e), (i), (m) Required rotation profiles to generate focused vortex beams with the topological charges of $l = 1, 2, 3, 4$, respectively. (b), (f), (j), (n) Measured electric intensity ($|R_{rr}|^2$) distributions and (c), (g), (k), (o) measured phase ($\angle R_{rr}$) distributions of different vortex beams, respectively, obtained at the focal plane. (d), (h), (l), (p) OAM amplitude $|S_n|$ extracted from the measured complex amplitudes of different vortex beams, respectively.

If the target functionalities are metalensings, their corresponding negative phase distributions ($-\Phi_{L,2}$ and $-\Phi_{R,1}$) correspond to divergences and thus have slight influences on the focusing spots achieved by positive phase distributions ($\Phi_{R,1}$ and $\Phi_{L,2}$). For instance, Fig. S12 in the Supplementary Material experimentally shows that the proposed metasurface can focus the $|R_{rr}|^2$ of 6.3 GHz and $|R_{ll}|^2$ of 7 GHz at different positions. For multiplexing further complicated functionalities, the crosstalk from unwanted parts becomes serious. If only the intensity profile of the target functionality is important (such as metalensing and holography), the phase profiles of $\Phi_{R,1}$ and $\Phi_{L,2}$ can be carefully optimized to reduce the crosstalk.[67] Nevertheless, to delink the multiplexed functionalities for RCP and LCP channels, due consideration must be paid into the spin-independent design freedom, such as propagation phase (see Supplementary Material 13 for details).
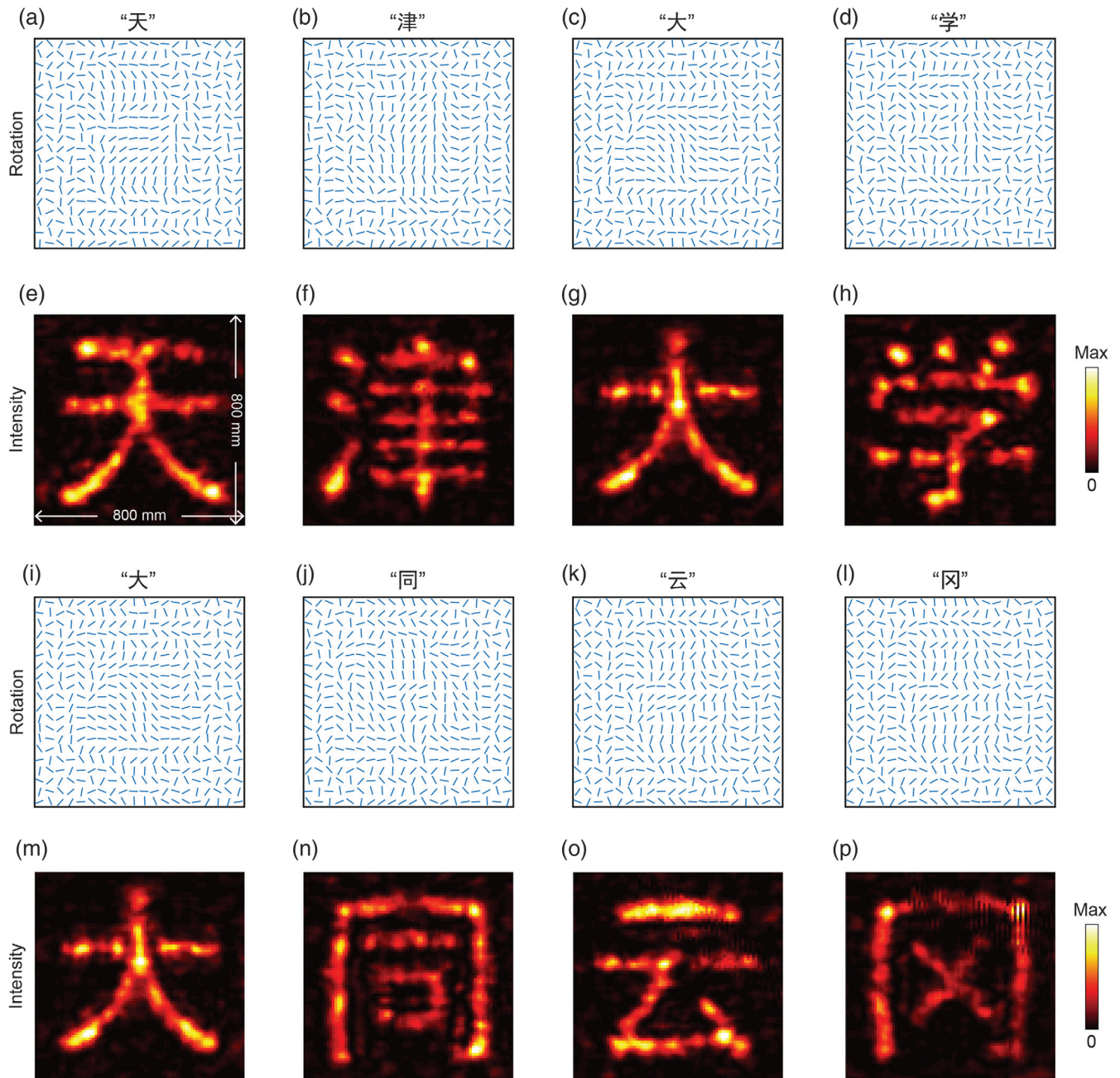
**Fig. 5** Holographic imaging. (a)–(d), (i)–(l) Required rotation profiles to generate holographic images of Chinese characters "天津大学" (Tianjin University) and "大同云冈" (Datong Yungang), respectively. (e)–(h), (m)–(p) Corresponding measured electric field intensities ($|R_{rr}|^2$) of holographic images obtained at $z = 600$ mm.

## 4 Discussion and Conclusion

We have demonstrated a reprogrammable mechanical PB metasurface platform and showcased its superior dynamic and efficient control of the impinging wavefront by reconfiguring in real time its operation across a number of functionalities. From the diffraction optics perspective, the performance of our optical metasurface gradually converges to the ideal response as the phase control level increases. Supplementary Material 14 uses metalensing as an example and numerically compares the performance of 2-level, 4-level, quasicontinuous (28-level),

and ideal phase control schemes, showing that the focus intensity of our quasicontinuous scheme is nearly identical to the ideal one, about 2.61 and 1.25 larger than the case of 2- and 4-level phase control schemes, respectively. In the current design, the meta-atoms in the same supercell are designed to have the same orientation angle, where the gear set identically transmits the torque from the stepping motor to each meta-atom. Since the mechanically reprogrammable modules and meta-atoms can be flexibly attached/detached from the metasurface, the proposed metasurface platform can conveniently incorporate different gear sets and different meta-atoms, which may

empower multidimensional manipulation of electromagnetic waves with programmability (see Supplementary Material 13 for details).

Modulation frequency is also an important metric of reprogrammable metasurfaces. Among the voltage-driven elements-based metasurfaces, the reported fastest modulation frequency could achieve 10 MHz.[54] Microfluidic[59] and mechanical[61] tuning is generally slow. With our metasurface, the rotation speed of the PB meta-atom is determined by the rotating speed of the step motor, the rotation ratio of the gear set, and the geometric phase dependence coefficient. In the current design, the rotation speed of stepping motors is set as ~2 s per turn, the rotation ratio of the gear set is 8/7, and the PB phase dependence coefficient is ±2, corresponding to a modulation frequency of about 8/7 Hz. It should be emphasized that by adopting step motors with a higher speed, gear sets with a larger rotation ratio, and meta-atoms with high-fold rotational symmetries,[63] the PB phase modulation frequency can be much improved. Such speed, although it is still slower than what can be achieved using voltage-driven diodes, can meet the requirement of some important applications, such as dynamic optimization of wireless communication channels,[47,49,51] intelligent imager/recognizer,[40,45] and self-adaptive cloak,[46] since they aim to reconfigure functionality according to variations of weather, temperature, and the motion of pedestrian or stealth vehicles. On the other hand, the proposed mechanical metasurface features low power dissipation (lower than 37.5 milliwatts at the meta-atom level) and nonvolatility, and therefore it is energy-saving and environment-friendly for large-scale and long-term applications.

For the applications that directly launch designated microwave beams, say the military radar system that steers a beam quickly across the sky to detect planes, the well-established phased arrays are more suitable. In contrast, the reprogrammable metasurfaces, either diodes-based metasurfaces or the proposed mechanical metasurface, aim to interact with incident beams and then tailor the out beams, playing the role as a part of the communication channels or surroundings. Therefore, from the function aspect, reprogrammable metasurfaces are more suitable for applications that are designed to control the wavefront of an external source of radiation, such as dynamic optimization of wireless communication channels[47,49,51] or self-adaptive cloak.[46] With our metasurface, the low power dissipation and the nonvolatility are also key for the cloak: the low power dissipation leads to low heat generation, which reduces the risk of detection by infrared technology; the nonvolatility makes the stealth vehicles possible for being hidden a long time and on standby with a relative low energy consumption. It also should be emphasized that each kind of technology has different performances in multiple dimensions. Such diversity ensures each technology has its own place in future applications, and on the other end will encourage continuous endeavors to optimize each specific technology for most suitable scenario.

In summary, we have demonstrated a versatile approach to implement a mechanically reprogrammable PB metasurface with superior performance. In principle, this metasurface can be reconfigured to yield various functionalities of choice. High-performance functionalities can be dynamically switched by this cost-effective metasurface, which is of great interest in various microwave applications. Precise and reversible control of micro/nanoelements in space and time has long been pursued in the context of micro/nanotechnologies.[68–71] We envision that our work may further boost endeavors into the interdisciplinary

fields between micro/nanotechnologies to push these concepts to higher frequencies, enabling precise rotation control of micro/nanoscale PB meta-atoms with full addressability and programmability to compress optical reprogrammable metasurfaces into a single chip.

# 5 Appendix: Measurements

In experiments, a VNA was used to acquire the response data by measuring the transmission coefficients ($S_{21}$). During measurements, the feed horn antenna and receive antenna/probe are connected to the output and input ports, respectively, of the VNA through two 3-m-long 50 Ω coaxial cables. The excitation source is a linearly polarized wave emitted by the feeding antenna with a working bandwidth from 2 to 18 GHz. The experimental results shown in Fig. 2 are obtained by adopting a broadband antenna (the same as the feeding antenna) as the receiver. By respectively rotating the feed and receive antenna, the reflection coefficients for different linearly polarized waves, i.e., $R_{xx}, R_{xy}, R_{yx}$, and $R_{yy}$, can be obtained, then the reflection coefficients for circularly polarized waves can be calculated using the transformation

$$
\begin{pmatrix} R_{rr} & R_{rl} \\ R_{lr} & R_{ll} \end{pmatrix}
= \frac{1}{2} \begin{pmatrix} R_{xx} - R_{yy} + i(R_{xy} + R_{yx}) & R_{xx} + R_{yy} - i(R_{xy} - R_{yx}) \\ R_{xx} + R_{yy} + i(R_{xy} - R_{yx}) & R_{xx} - R_{yy} - i(R_{xy} + R_{yx}) \end{pmatrix}.
$$

(1)

The experimental results shown in Figs. 3–5 are obtained by adopting a waveguide probe as the receiver. Driven by an electric-controlled translation stage, the waveguide probe raster scans the linearly polarized waves over a large area, and the field distributions of ($|R_{rr}|^2$) are also calculated by Eq. (1). For reference, Fig. S17 in the Supplementary Material shows the photos and schematics of the experimental setups.

*Data availability*

The data that support the plots of this study are available from the corresponding author upon reasonable request.

## References

1. W. T. Chen, A. D. Y. Zhu, and F. Capasso, "Flat optics with dispersion-engineered metasurfaces," *Nat. Rev. Mater.* **5**(8), 604–620 (2020).

2. P. Genevet et al., "Recent advances in planar optics: from plasmonic to dielectric metasurfaces," *Optica* **4**(1), 139–152 (2017).

3. X. Q. Zhang et al., "Terahertz surface plasmonic waves: a review," *Adv. Photonics* **2**(1), 014001 (2020).

4. F. Monticone and A. Alù, "Metamaterial, plasmonic and nanophotonic devices," *Rep. Prog. Phys.* **80**(3), 036401 (2017).

5. X. G. Luo et al., "Subwavelength interference of light on structured surfaces," *Adv. Opt. Photonics* **10**(4), 757–842 (2018).

6. B. Sain, C. Meier, and T. Zentgraf, "Nonlinear optics in all-dielectric nanoantennas and metasurfaces: a review," *Adv. Photonics* **1**(2), 024002 (2019).

7. G. Zheng et al., "Metasurface holograms reaching 80% efficiency," *Nat. Nanotechnol.* **10**(4), 308–312 (2015).

8. X. Zhang et al., "Direct polarization measurement using a multiplexed Pancharatnam–Berry metahologram," *Optica* **6**(9), 1190–1198 (2019).

9. S. Wang et al., "Broadband achromatic optical metasurface devices," *Nat. Commun.* **8**(1), 187 (2017).

10. M. Khorasaninejad et al., "Metalenses at visible wavelengths: diffraction-limited focusing and subwavelength resolution imaging," *Science* **352**(6290), 1190–1194 (2016).

11. R. C. Devlin et al., "Arbitrary spin-to-orbital angular momentum conversion of light," *Science* **358**(6365), 896–901 (2017).

12. Y. Yuan et al., "Independent phase modulation for quadruplex polarization channels enabled by chirality-assisted geometric-phase metasurfaces," *Nat. Commun.* **11**(1), 4186 (2020).

13. N. Yu et al., "Light propagation with phase discontinuities: generalized laws of reflection and refraction," *Science* **334**(6054), 333–337 (2011).

14. S. Sun et al., "Gradient-index meta-surfaces as a bridge linking propagating waves and surface waves," *Nat. Mater.* **11**(5), 426–431 (2012).

15. C. Pfeiffer and A. Grbic, "Metamaterial Huygens' surfaces: tailoring wave fronts with reflectionless sheets," *Phys. Rev. Lett.* **110**(19), 197401 (2013).

16. L. Liu et al., "Broadband metasurfaces with simultaneous control of phase and amplitude," *Adv. Mater.* **26**(29), 5031–5036 (2014).

17. Q. Xu et al., "Polarization-controlled surface plasmon holography," *Laser Photonics Rev.* **11**(1), 1600212 (2017).

18. Q. Fan et al., "Independent amplitude control of arbitrary orthogonal states of polarization via dielectric metasurfaces," *Phys. Rev. Lett.* **125**(26), 267402 (2020).

19. A. Arbabi et al., "Dielectric metasurfaces for complete control of phase and polarization with subwavelength spatial resolution and high transmission," *Nat. Nanotechnol.* **10**(11), 937–943 (2015).

20. J. P. Balthasar Mueller et al., "Metasurface polarization optics: independent phase control of arbitrary orthogonal states of polarization," *Phys. Rev. Lett.* **118**(11), 113901 (2017).

21. F. Ding et al., "Versatile polarization generation and manipulation using dielectric metasurfaces," *Laser Photonics Rev.* **14**(11), 2000116 (2020).

22. B. Yang et al., "High-performance meta-devices based on multilayer meta-atoms: interplay between the number of layers and phase coverage," *Sci. Bull.* **64**(12), 823–835 (2019).

23. Q. He et al., "High-efficiency metasurfaces: principles, realizations, and applications," *Adv. Opt. Mater.* **6**(19), 1800415 (2018).

24. Y. B. Zhang et al., "Multidimensional manipulation of wave fields based on artificial microstructures," *Opto-Electron. Adv.* **3**(11), 200002 (2020).

25. A. Nemati et al., "Tunable and reconfigurable metasurfaces and metadevices," *Opto-Electron. Adv.* **1**(5), 18000901 (2018).

26. Q. He, S. Sun, and L. Zhou, "Tunable/reconfigurable metasurfaces: physics and applications," *Research* **2019**(2), 1849272 (2019).

27. N. I. Zheludev and E. Plum, "Reconfigurable nanomechanical photonic metamaterials," *Nat. Nanotechnol.* **11**(1), 16–22 (2016).

28. J. Gu et al., "Active control of electromagnetically induced transparency analogue in terahertz metamaterials," *Nat. Commun.* **3**(1), 1151 (2012).

29. H. T. Chen et al., "Experimental demonstration of frequency-agile terahertz metamaterials," *Nat. Photonics* **2**(5), 295–298 (2008).

30. B. Gholipour et al., "An all-optical, non-volatile, bidirectional, phase-change meta-switch," *Adv. Mater.* **25**(22), 3050–3054 (2013).

31. L. Mao et al., "Reversible switching of electromagnetically induced transparency in phase change metasurfaces," *Adv. Photonics* **2**(5), 056004 (2020).

32. X. Liu et al., "Thermally dependent dynamic meta-holography using a vanadium dioxide integrated metasurface," *Adv. Opt. Mater.* **7**(12), 1900175 (2019).

33. H. Tao et al., "Reconfigurable terahertz metamaterials," *Phys. Rev. Lett.* **103**(14), 147401 (2009).

34. M. Liu et al., "Temperature-controlled optical activity and negative refractive index," *Adv. Funct. Mater.* **31**(14), 2010249 (2021).

35. L. Ju et al., "Graphene plasmonics for tunable terahertz metamaterials," *Nat. Nanotechnol.* **6**(10), 630–634 (2011).

36. J. Y. Ou et al., "An electromechanically reconfigurable plasmonic metamaterial operating in the near-infrared," *Nat. Nanotechnol.* **8**(4), 252–255 (2013).

37. Y. Kim et al., "Phase modulation with electrically tunable vanadium dioxide phase-change metasurfaces," *Nano Lett.* **19**(6), 3961–3968 (2019).

38. Z. Q. Miao et al., "Widely tunable terahertz phase modulation with gate-controlled graphene metasurfaces," *Phys. Rev. X* **5**(4), 041027 (2015).

39. L. Li et al., "Electromagnetic reprogrammable coding-metasurface holograms," *Nat. Commun.* **8**(1), 197 (2017).

40. L. Li et al., "Machine-learning reprogrammable metasurface imager," *Nat. Commun.* **10**(1), 1082 (2019).

41. K. Chen et al., "A reconfigurable active Huygens' metalens," *Adv. Mater.* **29**(17), 1606422 (2017).

42. L. Zhang et al., "Space-time-coding digital metasurfaces," *Nat. Commun.* **9**(1), 4334 (2018).

43. X. Wan et al., "Multichannel direct transmissions of near-field information," *Light Sci. Appl.* **8**(1), 60 (2019).

44. H. Wu et al., "Harmonic information transitions of spatiotemporal metasurfaces," *Light Sci. Appl.* **9**(1), 198 (2020).

45. L. Li et al., "Intelligent metasurface imager and recognizer," *Light Sci. Appl.* **8**(1), 97 (2019).

46. C. Qian et al., "Deep-learning-enabled self-adaptive microwave cloak without human intervention," *Nat. Photonics* **14**(6), 383–390 (2020).

47. P. del Hougne, M. Fink, and G. Lerosey, "Optimally diverse communication channels in disordered environments with tuned randomness," *Nat. Electron.* **2**(1), 36–41 (2019).

48. X. G. Zhang et al., "An optically driven digital metasurface for programming electromagnetic functions," *Nat. Electron.* **3**(3), 165–171 (2020).

49. C. Liaskos et al., "A new wireless communication paradigm through software-controlled metasurfaces," *IEEE Commun. Mag.* **56**(9), 162–169 (2018).

50. J. W. You et al., "Reprogrammable plasmonic topological insulators with ultrafast control," *Nat. Commun.* **12**(1), 5468 (2021).

51. H. H. Yang et al., "A 1-bit 10 × 10 reconfigurable reflectarray antenna: design, optimization, and experiment," *IEEE Trans. Antennas Propag.* **64**(6), 2246–2254 (2016).

52. T. J. Cui et al., "Direct transmission of digital message via programmable coding metasurface," *Research* **2019**(e218), 2584509 (2019).

53. C. Huang et al., "Reconfigurable metasurface for multifunctional control of electromagnetic waves," *Adv. Opt. Mater.* **5**(22), 1700485 (2017).

54. L. Zhang et al., "A wireless communication scheme based on space- and frequency-division multiplexing using digital metasurfaces," *Nat. Electron.* **4**(3), 218–227 (2021).

55. T. J. Cui, S. Liu, and L. L. Li, "Information entropy of coding metasurface," *Light Sci. Appl.* **5**(11), e16172 (2016).
56. P. Thureja et al., "Array-level inverse design of beam steering active metasurfaces," *ACS Nano* **14**(11), 15042–15055 (2020).
57. C. H. Lin et al., "Automatic inverse design of high-performance beam-steering metasurfaces via genetic-type tree optimization," *Nano Lett.* **21**(12), 4981–4989 (2021).
58. S. Venkatesh et al., "A high-speed programmable and scalable terahertz holographic metasurface based on tiled CMOS chips," *Nat. Electron.* **3**(12), 785–793 (2020).
59. W. Zhu et al., "A flat lens with tunable phase gradient by using random access reconfigurable metamaterial," *Adv. Mater.* **27**(32), 4739–4743 (2015).
60. Z. Wang et al., "Origami-based reconfigurable metamaterials for tunable chirality," *Adv. Mater.* **29**(27), 1700412 (2017).
61. S. Liu et al., "Flexible controls of broadband electromagnetic wavefronts with a mechanically programmable metamaterial," *Sci. Rep.* **9**(1), 1809 (2019).
62. C. P. Jisha, S. Nolte, and A. Alberucci, "Geometric phase in optics: from wavefront manipulation to waveguiding," *Laser Photonics Rev.* **15**(10), 2100003 (2021).
63. X. Xie et al., "Generalized Pancharatnam–Berry phase in rotationally symmetric meta-atoms," *Phys. Rev. Lett.* **126**(18), 183902 (2021).
64. Q. Wang et al., "Reflective chiral meta-holography: multiplexing holograms for circularly polarized waves," *Light Sci. Appl.* **7**(1), 25 (2018).
65. Q. Wang et al., "Broadband metasurface holograms: toward complete phase and amplitude engineering," *Sci. Rep.* **6**(1), 32867 (2016).
66. W. T. Chen et al., "A broadband achromatic polarization-insensitive metalens consisting of anisotropic nanostructures," *Nat. Commun.* **10**(1), 355 (2019).
67. W. Ye et al., "Spin and wavelength multiplexed nonlinear metasurface holography," *Nat. Commun.* **7**(1), 11930 (2016).
68. H. Wang and M. Pumera, "Fabrication of micro/nanoscale motors," *Chem. Rev.* **115**(16), 8704–8735 (2015).
69. S. Mohith et al., "Recent trends in piezoelectric actuators for precision motion and their applications: a review," *Smart Mater. Struct.* **30**(1), 013002 (2021).
70. L. Xin et al., "A rotary plasmonic nanoclock," *Nat. Commun.* **10**(1), 5394 (2019).
71. A. Kuzyk et al., "Reconfigurable 3D plasmonic metamolecules," *Nat. Mater.* **13**(9), 862–866 (2014).

**Quan Xu** received his BEng degree in communication engineering and his MEng degree in optical engineering from Harbin Engineering University, China, in 2011 and 2014, respectively, and his PhD in optical engineering from Tianjin University, China, in 2019. He is currently an assistant professor at the Center for Terahertz Waves, Tianjin University, Tianjin, China. His research interests focus on metamaterial/metasurface devices, surface plasmons, and terahertz photonics.

**Xiaoqiang Su** received his BEng degree in physics from Yuncheng College, China, in 2009, his MEng degree in optics from Zhejiang Normal University, China, in 2012, and his PhD in optical engineering from Tianjin University, China, in 2016. He is currently an associate professor at the Institute of Solid State Physics, Shanxi Datong University, Datong, China. His research interests focus on reconfigurable intelligence surfaces and spoof surface plasmons.

**Xueqian Zhang** is an associate professor at Tianjin University, China. He received his BEng degree in electronic science and technology and his PhD in optical engineering from Tianjin University, China, in 2010 and 2016, respectively. He was a visiting scholar at the University of Birmingham, United Kingdom, and at King Abdullah University of Science and Technology, Saudi Arabia, from 2013 and 2014. His main research interests are terahertz metasurfaces, surface plasmonic waves, and nonlinear plasmonics.

**Lijuan Dong** received her BSc degree in physics from Yanbei Normal College, China, in 2000, her MSc degree in physics from Hebei University of Technology, China, in 2003, and her PhD in physics from Tongji University, China, in 2009. She is a full professor at the Institute of Solid State Physics, Shanxi Datong University, Datong, China. Her research interests focus on functional electromagnetic devices and wireless energy transfer technology.

**Lifeng Liu** received his BEng degree in physics from Shanxi Datong University, China, in 2006, his MEng degree in condensed matter physics from Chongqing University, China, in 2009, and his PhD in optical engineering from Chongqing University, China, in 2012. He is currently an associate professor at the Institute of Solid State Physics, Shanxi Datong University, Datong, China. His research interests focus on active metamaterial devices and spoof surface plasmon polaritons.

**Yunlong Shi** is currently a full professor at Shanxi Datong University. He received his PhD in condensed matter physics from Tongji University, China, in 1999. He was a visiting scholar at the Cavendish Laboratory of Cambridge University from 2003 to 2004. His research interests include photonic crystal, strongly correlated systems, and metamaterials.

**Qiu Wang** received his BEng degree in optoelectronic science and technology and his PhD in optical engineering from Tianjin University, China, in 2014 and 2020, respectively. He is currently an associate professor at the School of Information Engineering, Wuhan University of Technology, Wuhan, China. His current research mainly includes applications of the metasurfaces and optical calculation algorithms.

**Jiaguang Han** received his BSc degree in material physics from Beijing Normal University, China, in 2000, and his PhD in applied physics from Shanghai Institute of Applied Physics, Chinese Academy of Sciences, China, in 2006. From 2006 to 2007, he was a postdoctoral researcher at Oklahoma State University, United States. In 2007, he joined the National University of Singapore, Singapore, as a Lee Kuan Yew research fellow. He is a full professor and his research focuses on surface plasmon polaritons, metamaterials, and material studies in the terahertz regime.

**Weili Zhang** is a full professor at Oklahoma State University. He received his PhD in optical engineering from Tianjin University, China, in 1993. He was a postdoctoral research associate at the Hong Kong University of Science and Technology from 1993 to 1995. His research interests include terahertz optoelectronics, nano- and microstructured materials optics, and ultrafast phenomena. He is a fellow of OSA.

Biographies of the authors are not available.